



Constraints on (2060) Chiron's size, shape, and surrounding material from the November 2018 and September 2019 stellar occultations

F. Braga-Ribas, C L Pereira, B. Sicardy, J L Ortiz, J. Desmars, A. Sickafoose, M. Emilio, B. Morgado, G. Margoti, F L Rommel, et al.

► To cite this version:

F. Braga-Ribas, C L Pereira, B. Sicardy, J L Ortiz, J. Desmars, et al.. Constraints on (2060) Chiron's size, shape, and surrounding material from the November 2018 and September 2019 stellar occultations. *Astronomy and Astrophysics - A&A*, 2023, 676, pp.A72. 10.1051/0004-6361/202346749 . hal-04538191

HAL Id: hal-04538191




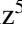



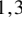




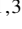

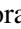


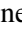
<https://hal.science/hal-04538191>

Submitted on 9 Apr 2024

HAL is a multi-disciplinary open access archive for the deposit and dissemination of scientific research documents, whether they are published or not. The documents may come from teaching and research institutions in France or abroad, or from public or private research centers.

L'archive ouverte pluridisciplinaire **HAL**, est destinée au dépôt et à la diffusion de documents scientifiques de niveau recherche, publiés ou non, émanant des établissements d'enseignement et de recherche français ou étrangers, des laboratoires publics ou privés.

Constraints on (2060) Chiron's size, shape, and surrounding material from the November 2018 and September 2019 stellar occultations

F. Braga-Ribas^{1,2,3} , C. L. Pereira^{4,3,1} , B. Sicardy² , J. L. Ortiz⁵ , J. Desmars^{6,7}, A. Sikafoose⁸ , M. Emilio⁹ ,
B. Morgado^{10,3} , G. Margoti^{1,3} , F. L. Rommel^{1,3} , J. I. B. Camargo^{4,3} , M. Assafin^{10,3} , R. Vieira-Martins^{4,3} ,
A. R. Gomes-Júnior^{11,3} , P. Santos-Sanz⁵ , N. Morales⁵ , M. Kretlow^{5,12} , J. Lecacheux² , F. Colas⁷,
R. Boninsegna¹², O. Schreurs^{13,14}, J. L. Dauvergne¹⁵ , E. Fernandez^{13,14}, H. J. van Heerden¹⁶, H. González¹⁷,
D. Bihel¹⁸, and F. Jankowsky¹⁹

(Affiliations can be found after the references)

Received 26 April 2023 / Accepted 12 June 2023

ABSTRACT

Context. After the discovery of rings around the largest known Centaur object, (10199) Chariklo, we carried out observation campaigns of stellar occultations produced by the second-largest known Centaur object, (2060) Chiron, to better characterize its physical properties and presence of material on its surroundings.

Aims. We aim to provide constraints on (2060) Chiron's shape for the first time using stellar occultations. We investigate the detectability of material previously observed in its vicinity using the 2018 occultation data obtained from South Africa Astronomical Observatory (SAAO).

Methods. We predicted and successfully observed two stellar occultations by Chiron. These observations were used to constrain its size and shape by fitting elliptical limbs with equivalent surface radii in agreement with radiometric measurements. We also obtained the properties of the material observed in 2011 with the same technique used to derive Chariklo's ring properties in our previous works, used to obtain limits on the detection of secondary events in our 2018 observation.

Results. Constraints on the (2060) Chiron shape are reported for the first time. Assuming an equivalent radius of $R_{\text{equiv}} = 105^{+6}_{-7}$ km, we obtained a semi-major axis of $a = 126 \pm 22$ km. Considering Chiron's true rotational light curve amplitude and assuming it has a Jacobi equilibrium shape, we were able to derive a 3D shape with a semi-axis of $a = 126 \pm 22$ km, $b = 109 \pm 19$ km, and $c = 68 \pm 13$ km, implying in a volume-equivalent radius of $R_{\text{vol}} = 98 \pm 17$ km. We determined the physical properties of the 2011 secondary events around Chiron, which may then be directly compared with those of Chariklo rings, as the same method was used. Data obtained from SAAO in 2018 do not show unambiguous evidence of the proposed rings, mainly due to the large sampling time. Meanwhile, we discarded the possible presence of a permanent ring similar to (10199) Chariklo's C1R in optical depth and extension.

Conclusions. Using the first multi-chord stellar occultation by (2060) Chiron and considering it to have a Jacobi equilibrium shape, we derived its 3D shape, implying a density of $1119 \pm 4 \text{ kg m}^{-3}$. New observations of a stellar occultation by (2060) Chiron are needed to further investigate the material's properties around Chiron, such as the occultation predicted for September 10, 2023.

Key words. comets: individual: (2060) Chiron – minor planets, asteroids: general – planets and satellites: rings – Kuiper belt: general

1. Introduction

After discovering rings around the Centaur object (10199) Chariklo, it was proposed that this feature may be common among distant small Solar System objects (Braga-Ribas et al. 2014). The centaur object (2060) Chiron is the second largest object of its kind. It has an equivalent diameter of 210^{+11}_{-14} km (model dependent), measured using data from the space telescopes *Spitzer* and *Herschel*, as well as from the Atacama Large Millimeter Array (ALMA; Lellouch et al. 2017).

Fundamental properties such as size and shape for objects of this kind can be obtained from Earth-based observations using stellar occultations (Ortiz et al. 2020)¹. High-cadence observations in terms of time and high signal-to-noise ratio (S/N) allow

for detecting or setting upper limits to the presence of material around the occulting body, for instance, on dust shells, jets, or rings (Elliot et al. 1995; Ortiz et al. 2020).

Secondary events on previous stellar occultation by (2060) Chiron have been reported for events in 1993, 1994, and 2011 (Bus et al. 1996; Elliot et al. 1995; Ruprecht et al. 2015). They were all interpreted as dust or jets coming from Chiron's surface, as it has presented periods of cometary activity (Tholen et al. 1988; Belskaya et al. 2010). In 1989, Meech & Belton (1989) were the first to detect a coma around Chiron. Later, Luu & Jewitt (1990) analyzed 1988–1990 data, further investigating Chiron's activity. As far as we know, no non-gravitational acceleration has been detected so far.

The November 29, 2011 occultation was observed using the Infrared Telescope Facility (IRTF), which detected the main body event, and from Faulkes Telescope North (FTN), which had a much higher cadence and S/N, but with no detection of the main body (Ruprecht et al. 2015). The latter data presented two

¹ An updated list of the detected stellar occultations by outer Solar System objects that we are aware of can be found at <http://occultations.ct.utfrp.edu.br/results> (Braga-Ribas et al. 2019).

Table 1. Observational circumstances of the September 8, 2019 Chiron occultation.

Site	Longitude E	Latitude N	Elevation (m)	Telescope aperture (mm)	Camera	Cycle ^(†) time (s)	σ_{flux}	Observers
Nandrin/BE	05 26 29.5	50 31 24.8	261	406	Watec-910HX	2.56	0.16	O. Schreurs, E. Fernandez
Dourbes/BE	04 34 56.0	50 05 25.9	195	400	Watec-910HX	1.28	0.23	R. Boninsegna
Ludiver/FR	−01 43 42.1	49 37 46.9	179	400	RAPTOR Kite	0.50	0.42	F. Colas, D. Bihel, J. Lecacheux
Paris/FR	02 20 26.5	48 49 26.9	79	250	ASI174MM	1.50	0.33	J. L. Dauvergne
Forcarei/ES	−08 22 15.2	42 36 38.4	670	507	Watec-910HX	2.56	0.11	H. González

Notes. ^(†)Read-out time is negligible for these cameras, so the exposure time equals the cycle time.

pairs of sharp secondary events that resembled those observed around Chariklo in 2013. These data were further analyzed by Sickafoose et al. (2020).

Ortiz et al. (2015) analyzed the reported absolute magnitude variation and the decrease of the amplitude of its rotation light curve, together with the secondary events relative to Chiron positions detected thus far, to argue that Chiron may also have a ring system. The final word on the presence of rings around Chiron depends on new observations of a stellar occultation with high cadence and S/N or on a visit of a spacecraft such as *Centaurus* (Singer et al. 2019).

In this work, we presented the first multi-chord stellar occultation by Chiron, observed on September 8, 2019, from four different sites. It gives further constraints on Chiron's size and shape. We also present a single chord detection observed from South Africa Astronomical Observatory (SAAO) on November 28, 2018, setting an upper limit on the detection of secondary events.

2. Stellar occultation of September 08, 2019

This stellar occultation event was predicted by the Lucky-Star project² using the Numerical Integration of the Motion of an Asteroid (NIMA), as described in Desmars et al. (2015), and the second *Gaia* Data Release (DR2) catalog (Gaia Collaboration 2018). The prediction path was updated using the astrometric position obtained at Pico dos Dias and Calar Alto Observatories and the astrometric position derived from the November 2018 occultation event (see Sect. 3).

The occulted star has the number 2741744913738549760 on the third *Gaia* Data Release (DR3) with a G magnitude of 16.52. The event had a shadow velocity of 22.8 km s^{-1} , relative to the geocenter. The position of the star from the *Gaia* DR3 catalog was propagated using parallax and proper motion to the event date, resulting in the following geocentric position at the epoch:

$$\alpha = 00^{\text{h}}10^{\text{m}}12^{\text{s}}.74303 \pm 0.1600 \text{ mas},$$

$$\delta = +04^{\circ}37'04''.9141 \pm 0.2824 \text{ mas},$$

where mas stands for milliarcsec.

An observation campaign was organized and observations were eventually made from five sites. The observation setups can be found in Table 1. Two sites in France (Ludiver and Paris)

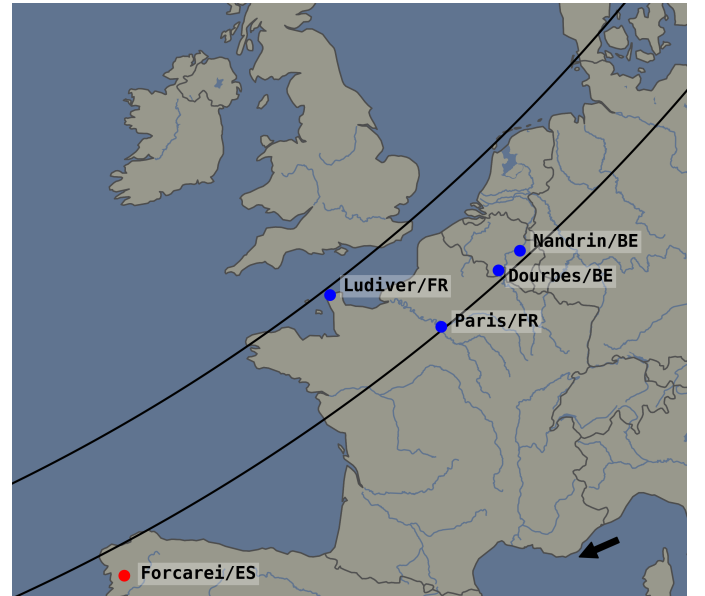


Fig. 1. Post-diction map of the event observed on September 8, 2019. The arrow at the bottom right indicates the motion of the shadow. The black lines represent Chiron's shadow path, the blue dots are the sites that detected the occultation, and the red one shows where data were acquired but no event was detected.

and two in Belgium (Nandrin and Dourbes) positively detected the event (Fig. 1). Unfortunately, the Belgian sites were in the same line with respect to Chiron's shadow path. Therefore, even if both were used, only three effective chords were available to derive the object's visible limb at the event time. Observations from Forcarei/ES were negative, that is, it did not detect the occultation by Chiron since it was south of the actual shadow path.

The occultation light curves (see Appendix A) were obtained using differential aperture photometry using the Package for the Reduction of Astronomical Images Automatically (PRAIA; Assafin et al. 2011). The ingress and egress times were calculated by modeling the light curve considering a sharp-edge occultation model convolved with Fresnel diffraction, the apparent stellar diameter at the object's distance, and the finite exposure time of each data set (more details can be found in Braga-Ribas et al. 2013; Souami et al. 2020). The shortest

² <https://lesia.obspm.fr/lucky-star/>

Table 2. Event times and chord length of the four positive sites on September 8, 2019 occultation.

Site	Ingress (UTC)	Egress (UTC)	Chord length (km)
Dourbes/BE	23:04:12.10 \pm 0.42	23:04:17.79 \pm 0.70	138 \pm 13
Nandrin/BE	23:04:08.00 \pm 0.43	23:04:13.40 \pm 0.92	146 \pm 28
Ludiver/FR	23:04:27.96 \pm 0.22	23:04:33.94 \pm 0.42	135 \pm 11
Paris/FR ^(†)	23:04:20.39 \pm 0.56	23:04:25.47 \pm 0.79	116 \pm 22

Notes. ^(†)Times not shifted, see text.

integration time was 0.5 s at the Ludiver site, translating into 11.4 km per data point along the track. Considering that the stellar apparent diameter equals 0.08 km, estimated using its B , V , and K magnitudes and van Belle (1999) equations for a main sequence star, and the Fresnel scale at $D = 17.85$ au (astronomical units) is $L_f = \sqrt{\lambda D/2} = 0.932$ km, the light curves are smoothed mainly by the exposure time.

The timings of the event are presented in Table 2. Time-stamping was ensured to be referenced to the Universal Time Coordinate (UTC) on the order of a millisecond by Global Positioning System (GPS) devices for all stations, except at Paris/FR, which had no reliable time source. The observation at Planetarium Ludiver/FR was made using a Raptor CMOS Kite camera and TimeBox system (Gallardo et al. 2021) and registered the images in ser³ format. Nandrin/BE site used a GPSBoxSprite-VTI, and Dourbes/BE site used an International Occultation Timing Association Video Time Inserter (IOTA-VTI) system⁴, both with Wattec 910HX video cameras, and the avi video format was used for registering the images. Paris/FR used a ZWO ASI174MM camera and registered the event using ser file format. All the data sets were converted to individual fits frames using Tangra software version 3.7.3⁵. The video GPS times are inserted at the end of the video camera exposures, so the time of individual frames were subtracted by half an exposure time to give the time of the middle of the integration correctly (details in Benedetti-Rossi et al. 2016; Barry et al. 2015).

2.1. Fit of the elliptical limb

The corrected times were projected in the sky plane and used to determine Chiron's limb shape at the time of the occultation. It is possible to see in Fig. 2 that the Paris chord is clearly shifted with respect to the other sites. As it did not benefit from a reliable time source, we shifted it forward by 0.9 s by minimizing the dispersion of the fitted ellipses with respect to the chord extremities. Due to the distribution and errors of the detected chords, a wide range of ellipses can be fitted.

The most recent and accurate work on determining Chiron's size, available in the literature, combined thermal fluxes with mid/far infrared fluxes to derive Chiron's relative emissivity at radio (mm and sub-mm) wavelengths (Lellouch et al. 2017). We considered their spherical approach, which gives an area-equivalent diameter of 210^{+11}_{-14} km, as we understand it to be the most conservative one. For instance, the error bar of the size given by this model encloses all the other scenarios (e.g., different roughness and elliptical profile). We used the aforementioned

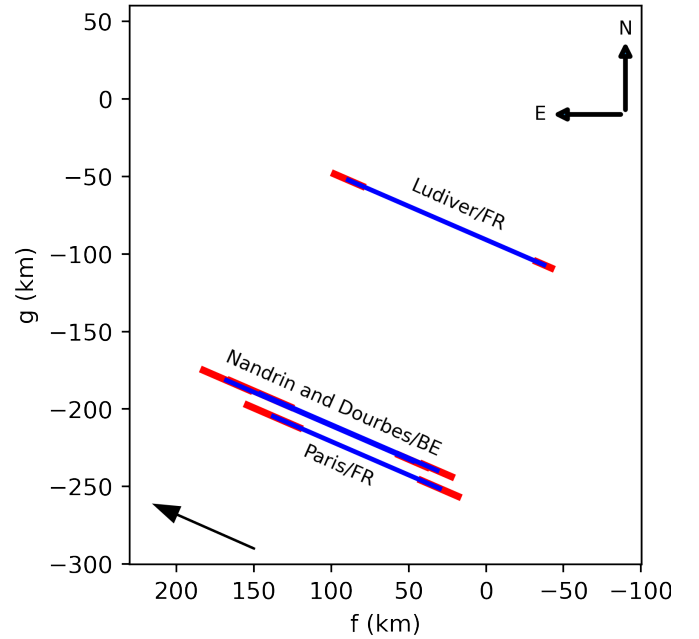


Fig. 2. Occultation chords in blue, with error bars in red, observed on September 08, 2019. From north to south, we have the chords from Ludiver/FR, Nandrin, and Dourbes/BE (same line), and Paris/FR. *Gaia* DR3 propagated star position and NIMA v10 provide the f_0 and g_0 during the geocenter's closest approach.

equivalent diameter as upper and lower limits on our fitting procedure to restrict the range of possible elliptical limbs compatible with our observed chords.

Our elliptical limb shape fitting to the occultation chords is detailed in Braga-Ribas et al. (2013) and Souami et al. (2020), for example. In short, we generated a large set of ellipses, varying their semi-major axes a' from 90 to 160 km by steps of 1 km, their oblatenesses $\epsilon = (a' - b')/a'$ (where a' and b' are the semi-major and semi-minor axis of the apparent ellipse) from 0 to 0.625 by steps of 0.005, and their Position Angles (PA)⁶ from -90° to $+90^\circ$ by steps of 2° . Moreover, in this procedure, we imposed that the area-equivalent radius, $R_{\text{equiv}} = a' \sqrt{1 - \epsilon}$, of the ellipse be consistent with the Lellouch et al. (2017)'s value within the error domain mentioned above, that is, $98 \leq R_{\text{equiv}} \leq 111$ km.

For each ellipse, the free parameters of the fit were the coordinates of body center (f_c, g_c) projected in the sky plane. This fit returned the classical χ^2 value based on the radial residuals of the fit, that is, the radial distance of the chord at the ingress/egress, $r_{i,\text{obs}}$, to the tested ellipse, $r_{i,\text{cal}}$, proportional to the radial uncertainty, σ_{radial} , of the ingress/egress time (Eq. (1)). The results

³ Simple uncompressed video format for astronomical capturing: <http://www.grischa-hahn.homepage.t-online.de/astro/ser/>

⁴ <https://occultations.org/>

⁵ <http://www.hristopavlov.net/Tangra3/>

⁶ The Position Angle is the angle between the celestial north and the minor-axis orientation, measured positively to the east.

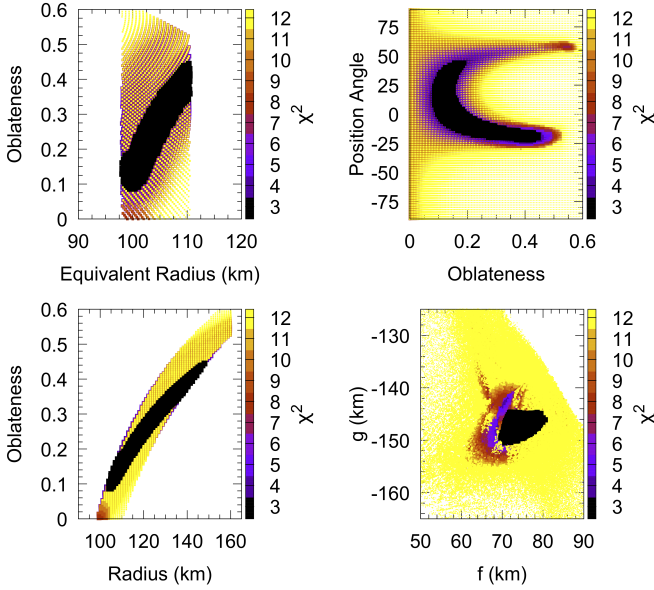


Fig. 3. Combinations of the limb-fitting parameters shown in each panel. The 1σ -level solutions are plotted in black. The solutions above this limit are shown in different colors, as defined in the color bar. Solutions above the 3σ are shown in yellow.

Table 3. Elliptic fit to the Chiron’s limb from the September 8, 2019 occultation.

Equivalent radius ^(†) (km)	$R_{\text{equiv}} = 105_{-7}^{+6}$
Semi-major axis (km)	$a = 126 \pm 22$
Position angle (deg)	$\text{PA} = 11 \pm 33$
Oblateness	$\epsilon = 0.27 \pm 0.18$

Notes. ^(†)Taken from Lellouch et al. (2017), see text.

were sorted from the minimum value χ^2_{min} , and for all the ellipses up to $\chi^2 + 1$ to define the marginal 1σ error bar of each parameter. The results are displayed in Fig. 3 for various parameters of interest.

$$\chi^2 = \sum_{i=1}^N \frac{(r_{i,\text{obs}} - r_{i,\text{cal}})^2}{\sigma_{\text{radial}}^2}. \quad (1)$$

Table 3 summarizes the results of the fit (limb’s size, shape, and orientation) and Fig. 4 displays the best ellipse in black and the 1σ -level solutions in gray.

2.2. Size and shape constraints

Although challenging due to the presence of coma and ring, rotational light curves have been observed for Chiron, giving a synodic rotation period of $P = 5.917813 \pm 0.000007$ h (Marcialis & Buratti 1993). Groussin et al. (2004) derived a true light curve amplitude of $\Delta m_0 = 0.16 \pm 0.03$, which is the light curve amplitude that we would observe if the object’s pole is perpendicular to the line of sight. This implies an axial ratio $b/a = \beta = 0.862 \pm 0.023$, for a triaxial body with axes $a > b > c$. Considering the pole direction given by Ortiz et al. (2015) to be the same as that of the main body, the opening angle (B) with respect to the object’s equator was $B = 42^\circ$ in 2019. So, the observed semi-major axis a of the ellipse can be considered as the actual equatorial radius of Chiron within a factor of 1.16 (at

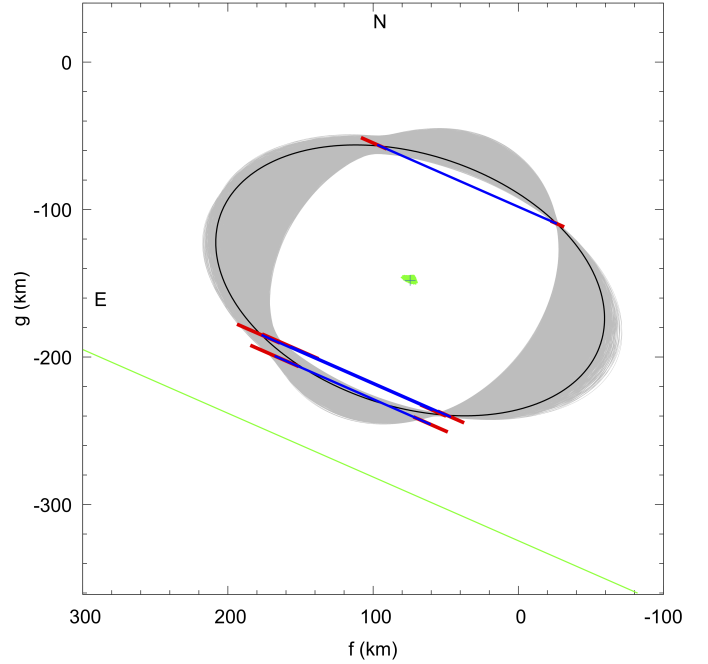


Fig. 4. Same as Fig. 2, with the best fitting ellipse plotted in black (e.g., the lowest χ^2 value) and the 1σ -level ellipse plotted in grey. The green spot in the center of the ellipses represents their respective centers. The Paris chord was shifted forward by 0.9 seconds for the best alignment with the other sites (see text for details). The green line below the ellipses is the negative chord observed from the Forcarei site.

maximum), given the known rotational variability and the fact that the rotational phase of Chiron at the time of the occultation was not known, implying that $b = 109 \pm 19$ km.

If Chiron has a Jacobi shape (i.e., fluid hydrostatic equilibrium), we can expect $c/a = \gamma = 0.53905 \pm 0.00785$ for a plausible density of $1,119 \pm 4 \text{ kg m}^{-3}$ and rotation period of $P = 5.917813 \pm 0.000007$ h, which would give a semi-minor axis of $c = 68 \pm 13$ km, using Chandrasekhar (1987) formalism. Under these assumptions, Chiron has a volume-equivalent radius of $R_{\text{vol}} = 98 \pm 17$ km.

We verified if the proposed ellipsoid agrees with the observed chords by assuming that Chiron has the same pole as the rings proposed by Ortiz et al. (2015) (i.e., the ring’s plane crosses the object’s equator). As the rotational phase during the 2019 event is unknown, we must test all the phases. Being ω the angle of the object’s major-axis (a) with respect to the intersection of the object’s equatorial plane and the International Celestial Reference System (ICRS) fundamental plane, as defined in Archinal et al. (2018), we note that values of ω in a range of 90° (i.e., one forth of a phase) provides compatible fits with the observed chords (Fig. 5). Figure 6 shows the best fit of Chiron as a Jacobi ellipsoid fitted to the 2019 occultation chords.

3. Stellar occultation of November 28, 2018

Also predicted by the Lucky Star project, this event was of interest due to the small shadow velocity of only 5.77 km s^{-1} , relative to the geocenter, thus allowing a high spatial resolution per data point. The occulted star was the *Gaia* DR3 2646598228351156352, with a magnitude $G = 17.28$. Propagating the position of the star from the *Gaia* DR3 catalog epoch using parallax and proper motion to the time of the event, its

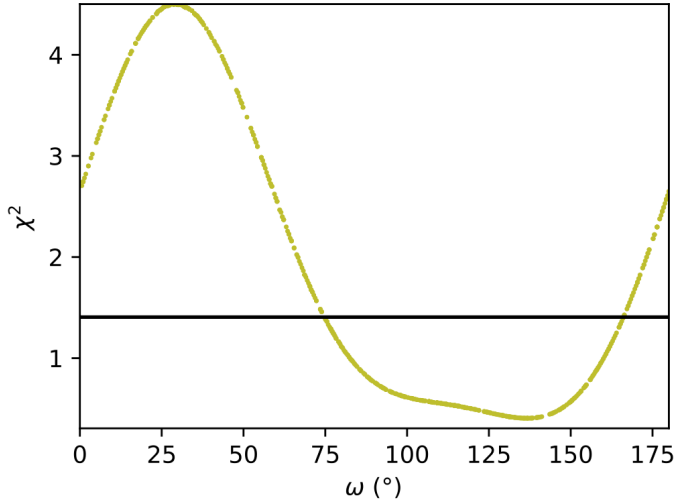


Fig. 5. Test of all possible rotation phases, considering Chiron as a Jacobi ellipsoid. Rotation phases within a range of 90° are compatible.

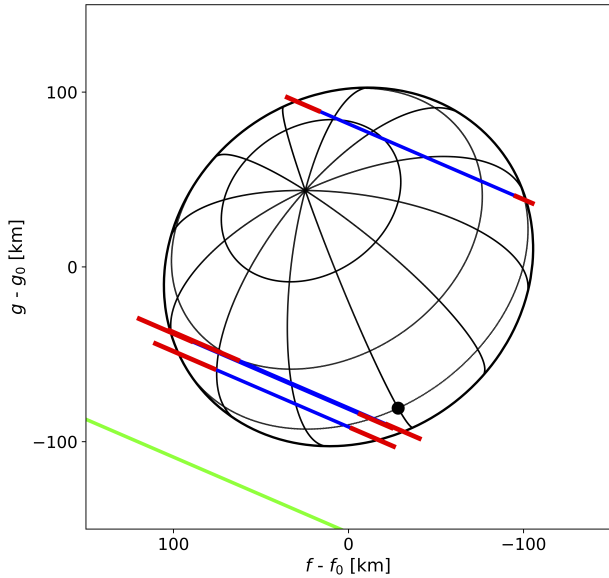


Fig. 6. Best fit of the Jacobi ellipsoid with $a = 126 \pm 22$ km, $b = 109 \pm 19$ km, and $c = 68 \pm 13$ km derived for Chiron, with a $\omega = 120^\circ$, represented by the big black dot, which also indicates the position of the major-axis a . Here, f_0 and g_0 are the center of the ellipse presented in Fig. 4.

geocentric position at epoch is:

$$\begin{aligned}\alpha &= 23^{\text{h}}46^{\text{m}}04^{\text{s}}.33575 \pm 0.2508 \text{ mas}, \\ \delta &= +02^\circ13'05''.5270 \pm 0.3445 \text{ mas}.\end{aligned}$$

Observations were arranged at the SAAO and at the Boyden Observatory, both in the Republic of South Africa. A third site was used in Namibia, the Automatic Telescope for Optical Monitoring (ATOM); (see [Hauser et al. 2004](#), for details on this facility). Table 4 provides circumstantial details and Fig. 7 displays the post-diction map.

The occultation could only be detected from SAAO. Using an exposure time of 1.5 seconds and no filter, each data point has a spatial resolution of 8.65 km and $S/R = 14$. Using the same procedures described in Sect. 2, the occultation light curve and the ingress and egress times were obtained (see Table 5). The stellar apparent diameter was estimated to be 0.3 km and

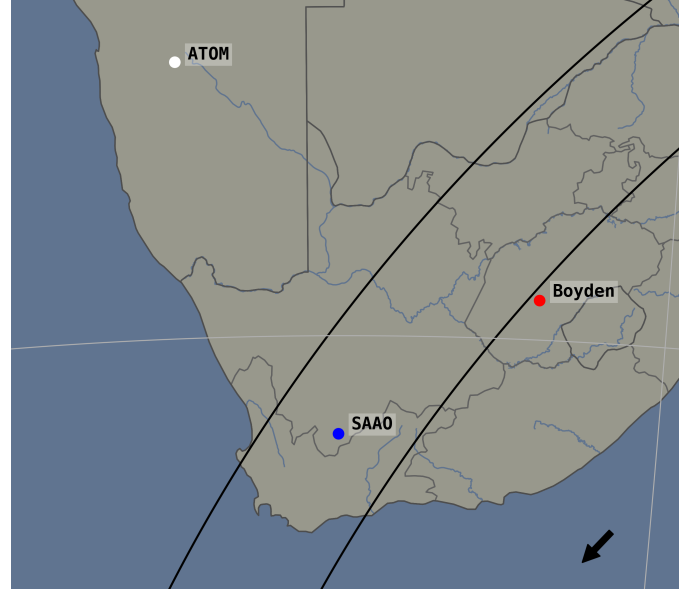


Fig. 7. Post-diction map of the November 28, 2018 event. The black lines delineate Chiron's shadow path, the blue dot is the SAAO site where the occultation was detected, the red dot is Boyden, where data were acquired but no event was detected, and the white dot (ATOM) could only start acquisition after the actual local closest approach.

the Fresnel scale at $D = 18.3538$ au is $L_f = 0.945$ km, so, again, the light curve smoothing was largely dominated by the exposure time.

The chords in the sky plane are displayed in Fig. 9. The large exposure time (10 s) used at Boyden Observatory smooths any putative short event, making it undetectable. Considering the long chord observed from SAAO, a long chord (at least one exposure time) would be detected from Boyden as well. As no flux drop was seen from there (Fig. A.1), we can conclude the center of Chiron was north of SAAO. This is a crucial constraint for the search of secondary events caused by the putative rings proposed by [Ortiz et al. \(2015\)](#).

4. Constraints on the secondary events

As mentioned earlier in this work, secondary events have been observed in the past during stellar occultations by Chiron ([Bus et al. 1996](#); [Elliot et al. 1995](#); [Ruprecht et al. 2015](#)) and it has been suggested that they may have been caused by a ring system, jets, or a dust shell ([Ortiz et al. 2015](#); [Sickafoose et al. 2020](#)). The only data set presented in this paper that offers useful limits on the detection of material around Chiron, while considering the image cadence and S/N, is the one obtained at SAAO in November 2018 (discussed further in this section).

4.1. Reanalysis of 2011 data

We re-assessed the physical properties of the features observed during the occultation by Chiron in 2011 ([Ruprecht et al. 2015](#)) when symmetrical secondary drops were detected around Chiron. Under the assumption that they are rings, as proposed by [Ortiz et al. \(2015\)](#), we followed the same procedures as those we used to analyze (10199) Chariklo's rings; (see [Braga-Ribas et al. 2014](#); [Bérard et al. 2017](#); [Morgado et al. 2021](#)).

Using the FTN data, as presented in Fig. 4 of [Ruprecht et al. \(2015\)](#) and reproduced in Fig. 2 of [Sickafoose et al. \(2020\)](#), we

Table 4. Observational circumstances of the November 28, 2018 Chiron occultation.

Site	Longitude E (° ' ")	Latitude S (° ' ")	Elevation (m)	Telescope aperture (mm)	Camera	Cycle ^(*) time (s)	σ_{flux}	Observers
SAAO	20 48 37.8	32 22 41.9	1760	1016	SHOC ^(‡)	1.5	0.08	A. Sickafoose
Boyden	26 24 17.0	29 02 19.8	1372	1500	Alta-U55	10	0.08	P. van Heerden
ATOM ^(†)	16 30 05.6	23 16 19.7	1800	700	DU888_BV	1.0	0.20	F. Jankowsky

Notes. ^(*)Read-out times are negligible for these cameras, so the exposure time equals the cycle time. ^(†)Observation initiated after the actual local closest approach. ^(‡)SHOC stands for Sutherland High-speed Optical Cameras, see [Copejans et al. \(2013\)](#).

Table 5. Derived event times and chord length as observed from SAAO on November 28, 2018.

Site	SAAO/SA
Ingress (UTC)	20:50:12.51 ± 0.06 s
Egress (UTC)	20:50:43.80 ± 0.10 s
Chord length	180.5 ± 0.9 km

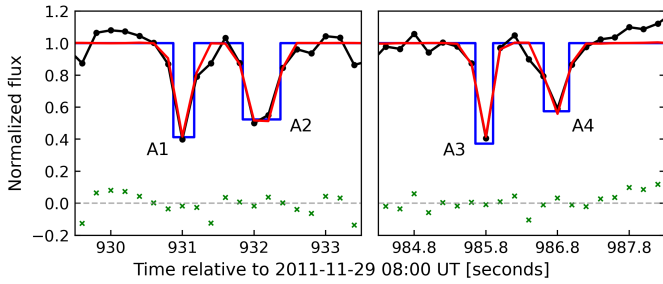


Fig. 8. Reanalysis of the FTN data obtained during the November 29, 2011 stellar occultation by Chiron; ([Ruprecht et al. 2015](#); [Sickafoose et al. 2020](#)). Adopting the preferred pole position proposed on [Ortiz et al. \(2015\)](#), we fit the light curves with two sharp-edged semi-transparent rings, accounting for the stellar velocity perpendicular to the ring as measured in the ring plane. Data are shown in black, the ring models are plotted in blue, and the red curves are the synthetic light curves, accounting for diffraction, stellar diameter, and finite integration time. The green crosses at the bottom are the fit residuals to the synthetic light curve. The times were corrected by -7 s with respect to the values published in [Ruprecht et al. \(2015\)](#) and [Sickafoose et al. \(2020\)](#), so they are back to their original values (see text).

first corrected the timing of those plots to their original values, which are presented in the above-mentioned references with a shift forward of 7 s to account for the geographic offset between FTN at Haleakala and IRTF at Mauna Kea. Using the preferred pole position of [Ortiz et al. \(2015\)](#), with ecliptic coordinates $\lambda = 144^\circ$, $\beta = 24^\circ$, we calculated the opening angle with respect to the object's equator (i.e., the sub-observer point), which was $B = 59.6^\circ$ in 2011, and the relative star velocities perpendicular to the rings, as measured in the ring plane. With these values, we fitted two sharp-edged rings with different sizes and opacity, accounting for diffraction (see the Extended Data in [Braga-Ribas et al. 2014](#); [Bérard et al. 2017](#), for further details). We tested ring widths varying from 0.5 to 4 km and opacity from 0 to 0.6. The resulting fits are shown in Fig. 8.

Table 6 shows the perpendicular velocity relative to the rings, $v_{\perp, \text{ring}}$, the mid-time of each detection, (t_{mid}), the apparent radial width, (W'), where “apparent” refers to the quantity measured in the sky plane, the radial width, (W_r), in the ring plane, the apparent opacity, ($p' = 1 - I/I_0$), the normal opacity to the ring plane,

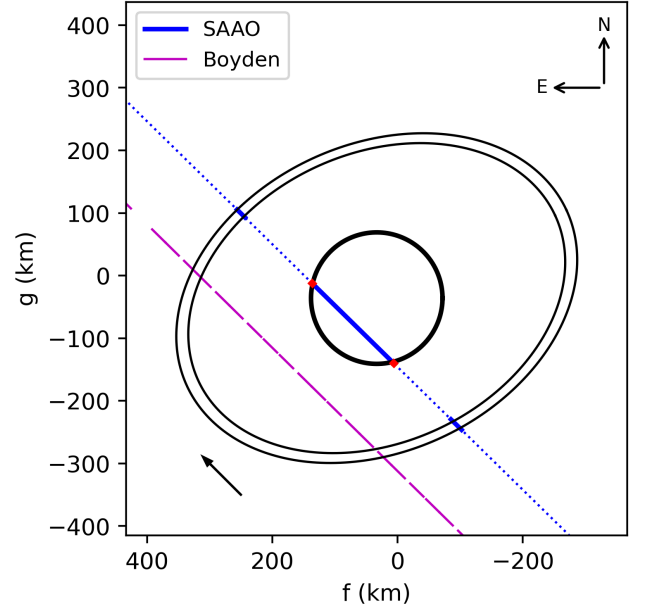


Fig. 9. Reconstructed geometry of 2018 event with the rings as proposed by [Ortiz et al. \(2015\)](#). The large blue segment corresponds to the chord detected from SAAO and the small ones are the expected location of the rings. The magenta dashed line corresponds to each exposure from the Boyden observatory negative chord.

($p_N = |\sin B|(1 - \sqrt{1 - p'})$), for a monolayer ring, the normal optical depth to the ring plane, ($\tau_N = |\sin B|(\tau'/2)$), for a polylayer ring, where $\tau' = -\ln(1 - p')$, and the equivalent width, ($E_p = W_r p_N$).

They are consistent with the values of [Sickafoose et al. \(2020\)](#) but differ due to (i) the applied velocity to calculate the widths and (ii) a factor of two between the apparent and the actual ring optical depths due to light diffraction by individual ring particles, as per [Cuzzi \(1985\)](#) and the discussion in [Bérard et al. \(2017\)](#). This factor of two applies in the cases where the Airy diffraction scale on individual particles with radius r $L_A \sim (\lambda/2r)D$, is larger than the width of the ring. In visible wavelengths and assuming ring particles with sizes of ten meters at most, this provides $L_A \geq 80$ km for $D = 18.3538$ au, hence validating our assumption (i.e., the actual ring optical depth is half of the one measured with the occultation light curve). Consequently, our equivalent width (E_p) values are almost half of those given by [Sickafoose et al. \(2020\)](#).

4.2. Searching for rings

To search for the proposed rings in the November 28, 2018 SAAO data set, we used the preferred pole position of [Ortiz et al. \(2015\)](#)

Table 6. Ring properties obtained from Faulkes 2011 data.

Ring properties from the 2011 detection				
	A1	A2	A3	A4
$v_{\perp \text{ring}}$ (km s ⁻¹)	7.18	6.99	8.67	8.73
t_{mid} (s) ^(†)	931.01 ± 0.02	932.06 ± 0.02	985.78 ± 0.01	986.80 ± 0.02
W' (km)	1.53 ± 0.15	2.38 ± 0.20	2.07 ± 0.37	3.27 ± 0.39
W_r (km)	2.22 ± 0.21	3.63 ± 0.29	1.98 ± 0.36	3.12 ± 0.37
p'	0.61 ± 0.06	0.47 ± 0.04	0.62 ± 0.06	0.40 ± 0.06
p_N	0.32 ± 0.04	0.23 ± 0.03	0.33 ± 0.04	0.20 ± 0.03
τ_N	0.41 ± 0.14	0.27 ± 0.08	0.42 ± 0.16	0.22 ± 0.09
E_p (km)	0.71 ± 0.11	0.85 ± 0.12	0.65 ± 0.14	0.61 ± 0.12

Notes. We used the same nomenclature as used by Sickafoose et al. (2020), where A1 and A2 correspond to the drops before the closest approach and A3 and A4 after the closest approach. ^(†) Seconds after 08:00 UT. Corrected by -7 s; see text.

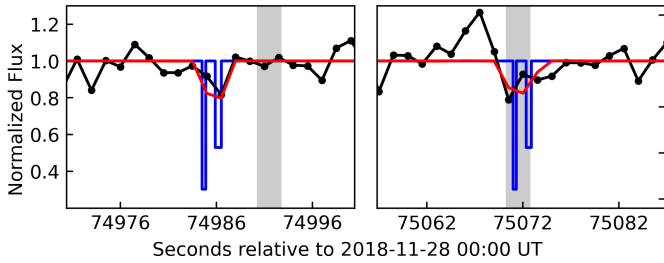


Fig. 10. Search for the Chiron's rings proposed by Ortiz et al. (2015) with the properties given by Sickafoose et al. (2020) using the SAAO data obtained during the November 28th 2018 occultation. The gray regions indicate the ring's expected positions from Ortiz et al. (2015). The left (resp. right) panel presents the data before (resp. after) the occultation by the main body.

($\lambda \sim 144^\circ$, $\beta \sim 24^\circ$) and the ring parameters derived from our re-analysis of the 2011 data (Table 6). From the event geometry (Fig. 9), we can estimate the time intervals where the proposed rings are expected (small blue segments).

Using the properties of the rings found in Sect. 4.1, we searched a region of 20 s (or ~ 115 km) around the expected rings locations, on both sides (before and after the main body ingress and egress). This corresponds to about seven times the total duration of the occultations by the rings and gap. The best fit for the ingress is obtained a few kilometers farther than the expected location (~ 36 km) and has a χ^2 value per degree of freedom of $\chi^2_{\text{pdf}} = 0.59$ (Fig. 10, left panel). For the egress, the best fits occur at the expected location, with a $\chi^2_{\text{pdf}} = 1.09$ (Fig. 10, right panel).

To assess the detection level of ring material, we analyzed the SAAO light curve, following the same procedures as in Bérard et al. (2017). We considered the data up to 2000 km from Chiron's center, excluding the main body occultation part. The light curve was converted into flux as a function of radial distance to the object's center, counted in the ring plane. Accounting for the standard deviation of the light curve, we obtained a 1σ upper limit of $p' = 0.08$ for the apparent opacity ($p' = 0.24$ at the 3σ level), see the red (resp. green) dashed line in Fig. 11. From the relation $\tau' = -\ln(1 - p')$, we derive an upper limit of $\tau' = 0.25$ (3σ level) for the apparent optical depth.

The star velocity at the ring plane was 7.99 km s⁻¹, yielding a spatial resolution of 12 km per data point. If existent, individual rings of this width would be detectable if $p_N = 0.09$ or $\tau_N > 0.09$. The proposed rings would then be detected at a 2.6σ level

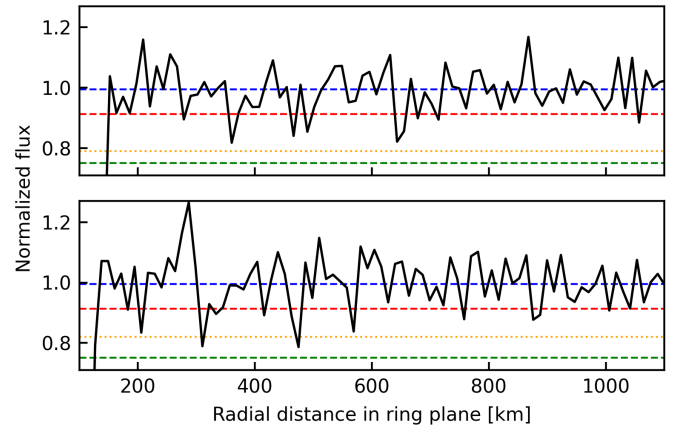


Fig. 11. Light curve of the flux versus the distance to Chiron's center in the ring plane. The dashed lines in red and green correspond to the detection limits at the 1 and 3σ levels, respectively. The yellow dotted line corresponds to the expected depth of the occultation promoted by the proposed rings.

during ingress and at a 2.2σ during egress (see the yellow dashed lines in Fig. 11). This means that the expected ring signatures were too weak to be assertively detectable in this data set with a 3σ or higher confidence level.

4.3. Searching for a shell of material

The SAAO data can also be used to put upper limits on the detection of a shell of material around Chiron. Using the same procedure as the previous section, the light curve was converted to flux versus distance to the object's center, but here the data were projected to the sky plane. Considering the standard deviation of the light curve, we obtain an apparent opacity of $p' = 0.08$ at the 1σ level and $p' = 0.24$ at the 3σ level, which represents an apparent optical depth of $\tau' = 0.25$ (3σ). Here, we considered the full resolution of 8.65 km allowed by the data set.

If we consider that a shell of material can be spread over a large region, we should also search for symmetrical drops over several kilometers radially to the object's center. To do so, we binned the data using windows of 45 and 81 km (according to the proposed structures in Elliot et al. 1995) and obtained apparent optical depth limits of $\tau' = 0.11$ and 0.08 at the 3σ level, respectively. As we can see in Figs. 12 and 13, no symmetrical or smooth flux drops are seen in both graph.

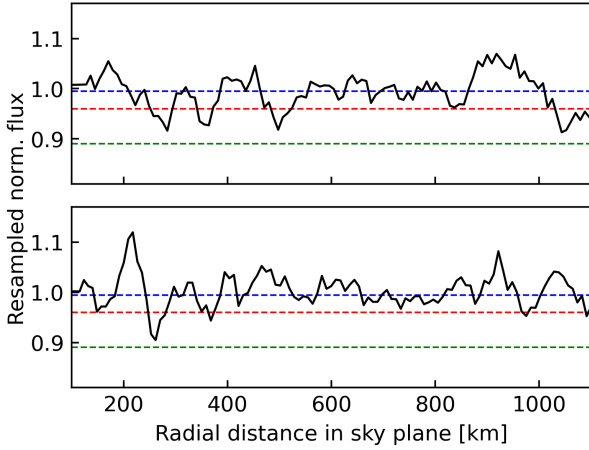


Fig. 12. Similar as Fig. 11, but the data were smoothed to a resolution of 45 km per data point.

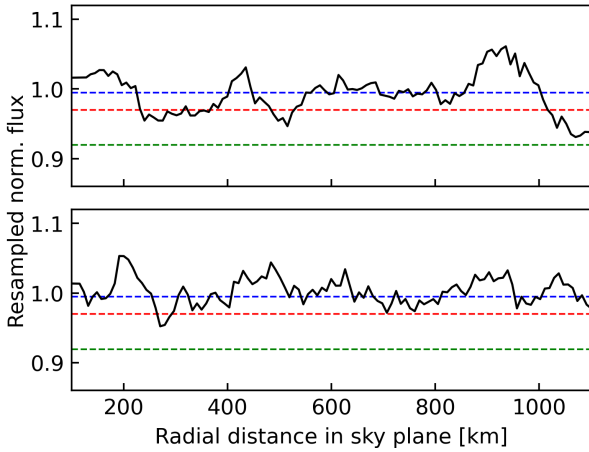


Fig. 13. Similar as Fig. 11, but the data were smoothed to a resolution of 81 km per data point.

5. Conclusions

We have presented here the first multi-chord stellar occultation by Chiron. Sizes determinations were made using different techniques before this work. For instance, Groussin et al. (2004) combined visible, infrared, and radio observations to derive a diameter of 142 ± 10 km; Fornasier et al. (2013) combined *Herschel* and *Spitzer* thermal data to derive (among other solutions) an equivalent diameter of 218 ± 20 km. Lellouch et al. (2017) reanalyzed the previous data adding observations made with ALMA to derive an equivalent diameter of 210 ± 10 km for a spherical model. They have also considered an elliptical model and the influence of the putative rings, but they found that neither help to reconcile the discrepant diameter determinations. We decided to use their spherical model as the most conservative approach and give reliable limits to Chiron's apparent equatorial diameter ($R_{\text{equat}} = 126 \pm 22$ km) and oblateness ($\epsilon = 0.27 \pm 0.18$).

Considering the derived true rotational light curve amplitude of $\Delta m_0 = 0.16 \pm 0.03$ (Groussin et al. 2004) and assuming a Jacobi shape (i.e., fluid hydrostatic equilibrium), we can expect Chiron's semi-axis to be $a = 126 \pm 22$ km, $b = 109 \pm 19$ km, and $c = 68 \pm 13$ km, implying a model-dependent density of $1119 \pm 4 \text{ kg m}^{-3}$, for a rotation period of 5.917813 h, and a volume-equivalent radius of $R_{\text{vol}} = 98 \pm 17$ km. With these values, we can obtain the first estimation of Chiron's mass of

Table 7. Chiron's astrometric positions from 2018 and 2019 occultations.

Event date (dd-mm-yyyy) Instant (UT) (hh:mm:ss.s)	Right ascension (hh mm ss.s) Declination (° ' ")	Astrometric uncertainty (mas)
28-11-2018 20:50:43.14	23 46 04.35419 +02 13 05.25822	± 0.26 ± 0.35
08-09-2019 23:04:26.20	00 10 12.73280 +04 37 05.26207	± 0.91 ± 0.45

$4.8 \pm 2.3 \times 10^{18}$ kg. When Chiron is viewed equator-on, the average equivalent surface radius is $R_{\text{Sequiv}} = 89 \pm 16$ km, it can be used with the true absolute magnitude of 7.28 ± 0.08 in V band obtained by Groussin et al. (2004) and $\text{Mag}_V = -26.74$ for the Sun, to calculate Chiron's geometric albedo to be $p_V = 0.076 \pm 0.026$, which is not in agreement with their value of 0.11 ± 0.02 ; however, as discussed by Ortiz et al. (2015), they did not consider the presence of the putative rings, which may contribute to up to 30% of the total reflected flux. Even if Chiron does not exhibit a Jacobi equilibrium shape, which might be the case, it is reasonable to consider that it does not diverge much from the here proposed shape.

We reanalyzed the secondary events observed in 2011 using Faulkes Telescope (Ruprecht et al. 2015; Sickafoose et al. 2020) and obtained the properties of the rings using the same procedures as Braga-Ribas et al. (2014); Bérard et al. (2017), considering the size and pole orientation proposed by Ortiz et al. (2015).

Data obtained from South Africa Astronomical Observatory allowed for a search for signatures of the proposed ring system. No clear evidence of the presence of the rings was found, mainly due to the long exposure time needed to record the occultation event. If the structures observed in 2011 were present in the 2018 data, they would have been detected at 2.6σ during the ingress and 2.2σ at the egress. These values are too low to claim any detection. Figure 11 clearly shows that many drops are below the 1σ level, but none below the 3σ level. We note that a ring such as the C1R, the main ring of (10199) Chariklo (Morgado et al. 2021), would have been detected above the 3σ level.

We also searched for broad features, such as a shell of material, and found no evidence. The upper limits are $\tau' = 0.25$, 0.11, and 0.08 for shells spread over ~ 9 , 45, and 81 km, respectively. Elliot et al. (1995) reported a feature (F2) with width ~ 74 km and a maximum optical depth of $\tau' \sim 0.11$. Considering the detection limit for apparent optical depth obtained with the 81 km-smoothed curves, the F2 feature would be detected outside the 3σ level.

Chiron is currently in a region of the sky characterized by a low density of stars, so relevant occultation events by this object are very rare. Thus, observations of new occultation events are needed. Adding the astrometric positions of the events presented here (Table 7) and those presented in Rommel et al. (2020), we searched for future events. A promising event will occur on September 10, 2023 (Fig. 14)⁷, which may allow for more precise size and shape determinations and contribute further information on Chiron's environment.

⁷ Further information can be found in the Lucky Star event's webpage <https://lesia.obspm.fr/lucky-star/occ.php?p=123202>

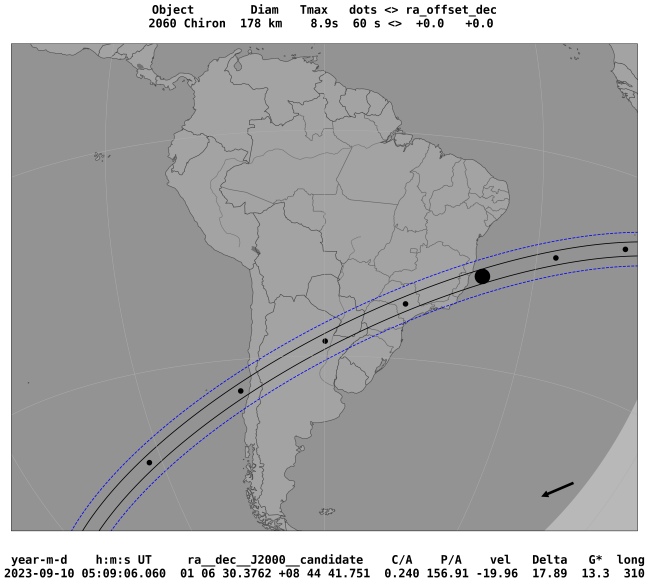


Fig. 14. Most promising upcoming occultation event by Chiron on September 10, 2023. Solid black lines correspond to the main body shadow path, while the blue dashed lines the projected distance of the proposed rings. Prediction based on the latest NIMA ephemeris (NIMAv15, available on the Lucky Star web page), using astrometric positions from all the detected occultations by Chiron and the *Gaia* DR3 catalog.

Acknowledgements. This work was carried out within the Lucky Star umbrella that agglomerates the efforts of the Paris, Granada, and Rio teams, which is funded by the European Research Council under the European Community H2020 (ERC Grant Agreement No. 669416). This study was financed in part by the Coordenação de Aperfeiçoamento de Pessoal de Nível Superior – Brasil (CAPES) – Finance Code 001 and the National Institute of Science and Technology of the e-Universe project (INCT do e-Universe, CNPq grant 465376/2014-2). The following authors acknowledge the respective CNPq grants: F.B.-R. 314772/2020-0; BEM 150612/2020-6; RV-M 307368/2021-1, 401903/2016-8; J.I.B.C. 308150/2016-3; M.A. 427700/2018-3, 310683/2017-3, 473002/2013-2. The following authors acknowledge the respective grants: C.L.P. thanks the FAPERJ/DSC-10 (E26/204.141/2022); B.E.M. thanks the CAPES/Cofecub-394/2016-05 grant; M.A. acknowledges F.A.P.E.R.J. grant E-26/111.488/2013; A.R.G.Jr acknowledges F.A.P.E.S.P. grant 2018/11239-8; Some of the results were based on observations taken at the 1.6 m telescope on Pico dos Dias Observatory of the National Laboratory of Astrophysics (L.N.A./Brazil). This research made use of SORA, a Python package for stellar occultations reduction and analysis, developed with the support of ERC Lucky Star and LIneA/Brazil. This work has made use of data from the European Space Agency (E.S.A.) mission *Gaia* (<https://www.cosmos.esa.int/gaia>), processed by the *Gaia* Data Processing and Analysis Consortium (D.P.A.C., <https://www.cosmos.esa.int/web/gaia/dpac/consortium>). J.L.O., P.S.-S., N.M., and M.K. acknowledge financial support from the grant CEX2021-001131-S funded by MCIN/AEI/10.13039/501100011033 and they also acknowledge the financial support by the Spanish grant nos. AYA-2017-84637-R and PID2020-112789GB-I00 and the Proyectos de Excelencia de la Junta de Andalucía grant nos. 2012-FQM1776 and PY20-01309.

References

Archinal, B. A., Acton, C. H., A'Hearn, M. F., et al. 2018, *Celest. Mech. Dyn. Astron.*, **130**, 22

Assafin, M., Vieira Martins, R., Camargo, J. I. B., et al. 2011, in *Gaia follow-up network for the solar system objects : Gaia FUN-SSO workshop proceedings*, 85

Barry, M. A. T., Gault, D., Pavlov, H., et al. 2015, *PASA*, **32**, e031

Belskaya, I., Bagnulo, S., Barucci, M., et al. 2010, *Icarus*, **210**, 472

Benedetti-Rossi, G., Sicardy, B., Buie, M. W., et al. 2016, *AJ*, **152**, 156

Bérard, D., Sicardy, B., Camargo, J. I. B., et al. 2017, *AJ*, **154**, 144

Braga-Ribas, F., Sicardy, B., Ortiz, J. L., et al. 2013, *ApJ*, **773**, 26

Braga-Ribas, F., Sicardy, B., Ortiz, J. L., et al. 2014, *Nature*, **508**, 72

Braga-Ribas, F., Crispim, A., Vieira-Martins, R., et al. 2019, *J. Phys. Conf. Ser.*, **1365**, 012024

Bus, S. J., Buie, M. W., Schleicher, D. G., et al. 1996, *Icarus*, **123**, 478

Chandrasekhar, S. 1987, *Ellipsoidal Figures of Equilibrium* (Hoboken: Wiley)

Coppejans, R., Gulbis, A. A. S., Kotze, M. M., et al. 2013, *PASP*, **125**, 976

Cuzzi, J. N. 1985, *Icarus*, **63**, 312

Desmars, J., Camargo, J. I. B., Braga-Ribas, F., et al. 2015, *A&A*, **584**, A96

Elliot, J. L., Olkin, C. B., Dunham, E. W., et al. 1995, *Nature*, **373**, 46

Fornasier, S., Lellouch, E., Müller, T., et al. 2013, *A&A*, **555**, A15

Gaia Collaboration (Brown, A. G. A., et al.) 2018, *A&A*, **616**, A1

Gallardo, C. V., Gault, D., & Midavaine, T., et al. 2021, *J. Occultation Astron.*, **11**

Groussin, O., Lamy, P., & Jorda, L. 2004, *A&A*, **413**, 1163

Hauser, M., Möllenhoff, C., Pühlhofer, G., et al. 2004, *Astron. Nachr.*, **325**, 659

Lellouch, E., Moreno, R., Müller, T., et al. 2017, *A&A*, **608**, A45

Luu, J. X., & Jewitt, D. C. 1990, *AJ*, **100**, 913

Marcialis, R. L., & Buratti, B. J. 1993, *Icarus*, **104**, 234

Meech, K. J., & Belton, M. J. S. 1989, *IAU Circ.*, **4770**, 1

Morgado, B. E., Sicardy, B., Braga-Ribas, F., et al. 2021, *A&A*, **652**, A141

Ortiz, J. L., Duffard, R., Pinilla-Alonso, N., et al. 2015, *A&A*, **576**, A18

Ortiz, J. L., Sicardy, B., Camargo, J. I., Santos-Sanz, P., & Braga-Ribas, F. 2020, in *The Trans-Neptunian Solar System*, eds. D. Pralnik, M. A. Barucci, & L. A. Young (Amsterdam: Elsevier), 413

Rommel, F. L., Braga-Ribas, F., Desmars, J., et al. 2020, *A&A*, **644**, A40

Ruprecht, J. D., Bosh, A. S., Person, M. J., et al. 2015, *Icarus*, **252**, 271

Sickafoose, A. A., Bosh, A. S., Emery, J. P., et al. 2020, *MNRAS*, **491**, 3643

Singer, K. N., Stern, S. A., Stern, D., Verbiscer, A., & Olkin, C. 2019, *EPSC-DPS Joint Meeting*, 2019, 2025

Souami, D., Braga-Ribas, F., Sicardy, B., et al. 2020, *A&A*, **643**, A125

Tholen, D. J., Hartmann, W. K., Cruikshank, D. P., et al. 1988, *IAU Circ.*, **4554**, 2

van Belle, G. T. 1999, *PASP*, **111**, 1515

- ¹ Federal University of Technology – Paraná (PPGFA/UTFPR-Curitiba), Rua Sete de Setembro, 3165, Curitiba, PR, Brazil
e-mail: fribas@utfpr.edu.br
- ² LESIA, Observatoire de Paris, Université PSL, CNRS, Sorbonne Université, Univ. Paris Diderot, Sorbonne Paris Cité, 5 place Jules Janssen, 92195 Meudon, France
- ³ Laboratório Interinstitucional de e-Astronomia – LIneA & INCT do e-Universe, R. General José Cristino 77, Bairro Imperial de São Cristóvão, Rio de Janeiro, RJ, Brazil
- ⁴ Observatório Nacional/MCTIC, R. General José Cristino 77, Bairro Imperial de São Cristóvão, Rio de Janeiro, RJ, Brazil
- ⁵ Instituto de Astrofísica de Andalucía, IAA-CSIC, Glorieta de la Astronomía s/n, 18008 Granada, Spain
- ⁶ Institut Polytechnique des Sciences Avancées IPSA, 63 boulevard de Brandebourg, 94200 Ivry-sur-Seine, France
- ⁷ Institut de Mécanique Céleste et de Calcul des Éphémérides, IMCCE, Observatoire de Paris, PSL Research University, CNRS, Sorbonne Universités, UPMC Univ Paris 06, Univ. Lille, 77 Av. Denfert-Rochereau, 75014 Paris, France
- ⁸ Planetary Science Institute, 1700 East Fort Lowell Road, Suite 106, Tucson, AZ 85719, USA
- ⁹ Universidade Estadual de Ponta Grossa, O.A. – DEGEO, Av. Carlos Cavalcanti, 4748, Ponta Grossa 84030-900, PR, Brazil
- ¹⁰ Observatório do Valongo/UFRJ, Ladeira Pedro Antônio 43, Rio de Janeiro, RJ, Brazil
- ¹¹ Institute of Physics, Federal University of Uberlândia, Av. João Naves de Ávila – 2121 – Santa Mônica, Uberlândia, MG, Brazil
- ¹² European Asteroidal Occultation Network (EAON), Rue de Mariembourg, 45, 5670 Dourbes, Belgium
- ¹³ International Occultation Timing Association – European Section (IOTA-ES), Am Brombeerhag 13, 30459 Hannover, Germany
- ¹⁴ Observatoire de Nandrin, Société Astronomique de Liège, Avenue des Platanes 17, 4000 Liège (Cointe), Belgium
- ¹⁵ Ciel et Espace, 17 rue Emile Deutsch de la Meurthe, 75014 Paris, France
- ¹⁶ University of the Free State, 205, Nelson Mandela Dr, Park West, Bloemfontein, 9301, South Africa
- ¹⁷ Observatorio astronómico de Forcarei, As Casetas, EP-7001, 18, 36556 Forcarei, Pontevedra, Spain
- ¹⁸ Planetarium Ludiver, 1700, rue de la Libération, Tonneville, 50460 La Hauge, France
- ¹⁹ Landessternwarte, Universität Heidelberg, Königstuhl 12, 69117 Heidelberg, Germany

Appendix A: Occultation Light Curves

The occultation light curves obtained from the here reported events are presented in Fig. A.1. The first four light curves from the 2019 event allowed to constrain Chiron's size and shape. The last light curve from the 2018 event allowed searching for secondary events around it.

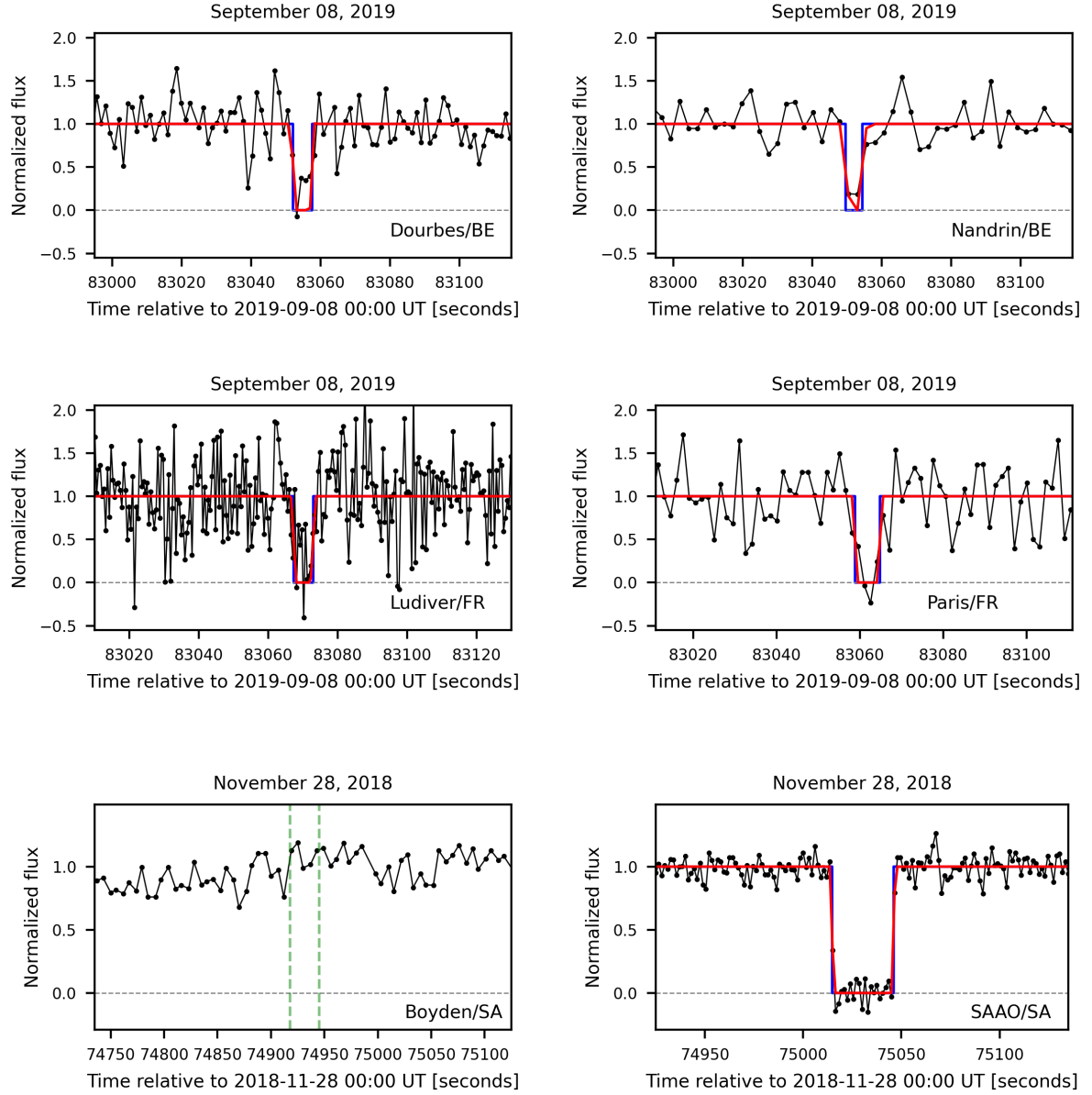


Fig. A.1. Black lines and dots are the data obtained from each site, the blue lines the opaque band, and red lines the modeled light curve, convoluted to the exposure time. Times are given in seconds after midnight of the event date. The site names are given in each panel. The green vertical dashed lines on Boyden's panel indicate the theoretical ingress and egress times.